



# A computationally efficient thermal modelling approach of the linear friction welding process



Clément Bühr\*, Paul A. Colegrove, Anthony R. McAndrew

Cranfield University, Cranfield, Bedfordshire MK43 0AL, UK

## ARTICLE INFO

### Keywords:

Linear friction welding

Modeling

Titanium alloy

## ABSTRACT

Numerical models used to simulate LFW rely on the modelling of the oscillations to generate heat. As a consequence, simulations are time consuming, making analysis of 3D geometries difficult. To address this, a model was developed of a Ti–6Al–4V LFW that applied the weld heat at the interface and ignored the material deformation and expulsion which was captured by sequentially removing row of elements. The model captured the experimental trends and showed that the maximum interface temperature was achieved when a burn-off rate of between 2 and 3 mm/s occurred. Moreover, the models showed that the interface temperature is reduced when a weld is produced with a higher pressure and when the workpieces are oscillated along the shorter of the two interface dimensions. This modelling approach provides a computationally efficient foundation for subsequent residual stress modelling, which is of interest to end users of the process.

## 1. Introduction

Linear friction welding is a solid-state joining process involving a stationary workpiece rubbed against another with a linear motion, under a compressive force to generate heat by friction and plastic deformation. The large deformation undergone by the material during the process usually results in a refined microstructure which can improve the properties of the weld relative to the parent material. Li et al. (2012) found an increase in the tensile strength at the joint when appropriate welding parameters are used. Wanjara and Jahazi (2005) recorded the highest hardness values at the weld centre for all the welding conditions considered. Wang et al. (2017) found evidence of anisotropic mechanical properties within titanium LFW due to the strong texture developed. Typically, less than 10 s are required to complete a titanium alloy weld using LFW, making it a fast welding process which also offers good repeatability. As detailed by Kumar (2013), LFW has been successfully implemented to weld titanium and nickel-based super alloy bladed-disks.

LFW was first divided into four phases by Vairis and Frost (1998) with the initial, transition, equilibrium and forging phases. During the initial phase, heat is generated by friction of the asperities located at the interfaces of the workpieces until the temperature is sufficient to create a viscoplastic layer, characteristic of the transition phase. At this point, the viscous material starts to be expelled from the interface creating flash. Most of the flash occurs during the equilibrium phase, where a quasi-steady state is reached for the interface force, thermal profile and burn-off rate. Once the desired upset is achieved, the two parts are

quickly and accurately aligned and a forging force is applied to consolidate the joint.

Owing to the rapid nature of LFW, it is difficult to get an insight into the process and as explained by Li et al. (2016) the choice of welding parameters have a significant impact on the heat generation and material flow. Therefore, many authors have used numerical modelling as an alternative to gain fundamental knowledge about LFW. Li et al. (2010) developed a 2D fully-coupled model which predicted a temperature of 1000 °C within 1 s of welding. However, no thermocouples recording were provided to validate the numerical predictions. Schroeder et al. (2012) demonstrated the dependency of the flash morphology upon the process parameters used, experiments and models exhibited a good match. McAndrew et al. (2015a, 2015b) used numerical models to evaluate the surface contaminant removal. A high applied pressure was recommended to minimise the amount of burn-off necessary to expel the contaminants. Numerical predictions were compared with metallographic images to observe the contaminant evolution. Turner et al. (2012) replicated numerically the welding conditions investigated by Romero et al. (2009) who conducted synchrotron X-ray diffraction experiments to predict the residual stress within LFW. Due to the lack of experimental data at the weld interface, it is unclear if peaks of residual stress are correctly predicted. Authors in the literature have attempted to model the complex mechanical mixing of LFW at the weld interface between the two parts. Unlike most other friction welding process, models of LFW in the literature are mostly fully-coupled. For example, Grant et al. (2009) developed a sequentially-coupled model simulating inertia friction welding where the

\* Corresponding author.

rotational motion of the process was not modelled. Thermal and mechanical predictions were found in a good agreement against experiments.

Three flow modelling approaches have been applied to LFW in the literature. The first approach developed by [Vairis and Frost \(2000\)](#) used a deformable body oscillated against a rigid body. Computational time was reduced with this approach; however a temperature dependant friction coefficient needs to be defined to account for the heat generation. Furthermore, the mechanical mixing occurring at the interface to form the joint cannot be modelled since only one body is deformed. Similar to the first approach, the second involves two deformable bodies rubbed against each other. Despite the use of two deformable bodies, the mechanical mixing is still not representative of the real process since the two interfaces do not merge. [Turner et al. \(2011\)](#) solved the problem by using a single body to represent the two original parts, and a thermal profile accounting for the heat input from the initial phases was mapped onto the mesh, allowing the material at the centre to deform. Using this approach [McAndrew et al. \(2015a, 2015b\)](#) successfully modelled the flash morphology for several welding conditions.

There are two dominant approaches to account for the heat generated during the welding phases within a numerical model. The first method uses a temperature dependant friction coefficient with a fully-coupled model to generate the heat during all the welding phases. [Blau \(2001\)](#) stated that the number of factors which potentially influence the friction coefficient is large and includes: contact geometry, fluid and flow properties, relative motion, applied forces, temperature and stiffness and vibrations. As a consequence, it is necessary to apply extra care when using friction coefficient values. The second method was first used by [McAndrew et al. \(2014\)](#) where the machine data recorded during welding were post-processed to determine the average heat flux over the initial phase. This was applied to a thermal model to predict the temperature distribution. After this, the single-body method mentioned above (developed by [Turner et al. \(2011\)](#)) was used to model the equilibrium phase, and an inelastic heat fraction was specified, typically in the range of 90–100% to represent the amount of mechanical work converted to heat. Both these approaches modelled the oscillations, so 3D models are computationally expensive and require weeks to complete a simulation as mentioned by [McAndrew et al. \(2016\)](#). Therefore, models are often limited to two dimensions and complex geometries cannot be considered.

The primary purpose of this paper is to present a novel modelling approach, experimentally verified, able to predict the temperature history of a linear friction weld that bypasses the modelling of the oscillations. Effects of rubbing velocity, burn-off rate, applied force and oscillation direction on the temperature histories are investigated.

## 2. Methodology

### 2.1. Experiments

Ti–6Al–4V linear friction welds were made at TWI Cambridge using the Thompson E20 machine for the five welding parameters listed in

**Table 1**  
Welding parameters.

Weld	Freq.	Amp.	Applied pressure	Burn-off	Rubbing velocity	Oscillation direction along the interface dimension:
	(Hz)	(mm)	(MPa)	(mm)	(mm/s)	
1	20	1.5	90	3	120	40 mm
2;6	30	2	90	3	240	40 mm
3	50	2.7	40	3	540	40 mm
4;7;8	50	2.7	90	3	540	40 mm
5	50	2.7	90	3	540	20 mm

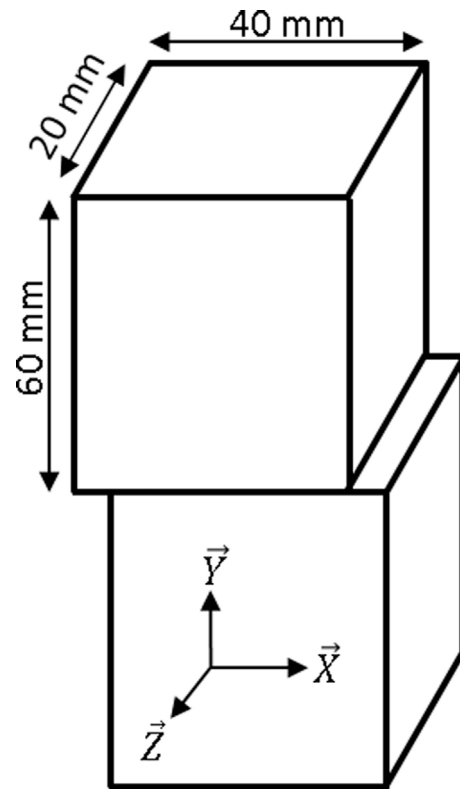


**Fig. 1.** Workpiece dimensions and axis.

**Table 1.** As shown in **Table 1**, some of the welding parameters were replicated to account for experimental variability. These welding parameters cover most of the operating window of frequency, amplitude and applied force of the LFW machine used. The experiments used workpieces measuring 20 × 40 × 60 mm, which is illustrated in **Fig. 1**. The Ti–6Al–4V parent material had a bimodal alpha-beta microstructure. Experimentally the workpiece was oscillated in the x direction (along the interface dimension 40 mm), except for weld 5 where it was oscillated transverse to this. Thermal histories were recorded during the welding process using k-type thermocouples with an outer diameter of 1 mm. EDM was used to produce the 1.2 mm diameter holes shown **Fig. 2(a)**. The thermocouples were inserted at depths of 0.3 mm, 1.2 mm, 2.7 mm, 4.2 mm and 5.2 mm from the weld interface and an epoxy resin was used to fix them in place. To get the thermocouple wires out of the clamping tool, a groove was machined on one workpiece, as shown in **Fig. 2(b)**.

The influence of the rubbing velocity was studied in the results section by comparing welds 1, 2 and 4. The average rubbing velocity, first defined by [Addison \(2008\)](#), is determined from the frequency  $f$  and amplitude  $A$  with  $v_r = 4Af$ . The effect of the applied force is examined using welds 3 and 4, while the oscillation direction is studied using welds 4 and 5.

During linear friction welding, several parameters were monitored with high-speed data acquisition systems including the oscillator position  $x$ , the in-plane force  $F_i$ , the axial position representing the burn-off and the applied force  $F_a$  applied on the non-oscillating workpiece, as shown in **Fig. 3**.

A similar approach to that developed by [Ofem et al. \(2010\)](#) and reemployed by [McAndrew et al. \(2015a, 2015b\)](#) was used for analysing the machine data. The machine data obtained during welding was post-processed and the average heat flux (Watt) per phase was calculated with the following formula:

$$\dot{Q}_{Phase} = \frac{\int_0^{T_{Phase}} F_{int} v dt}{T_{Phase}}$$

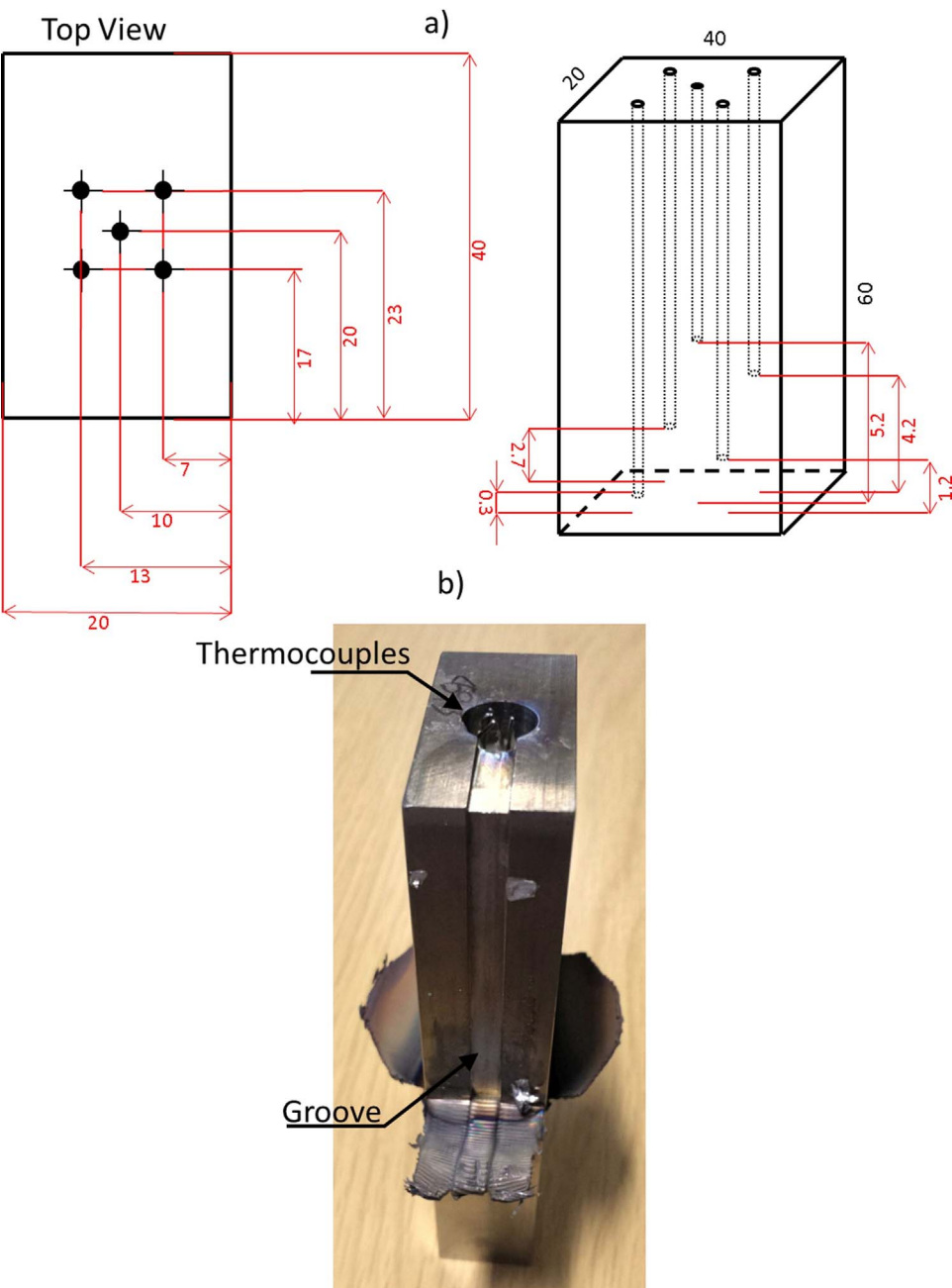


Fig. 2. a) Positioning of the thermocouples and b) experimental sample showing the hole where the thermocouples were fitted and the groove.

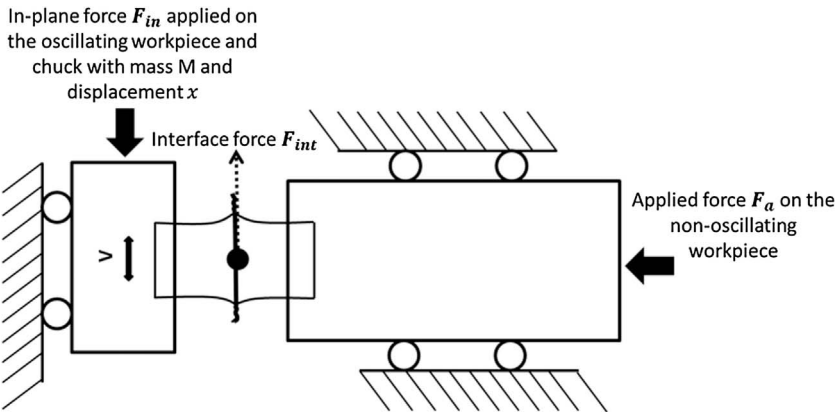


Fig. 3. Schematic illustration of the linear friction machine.

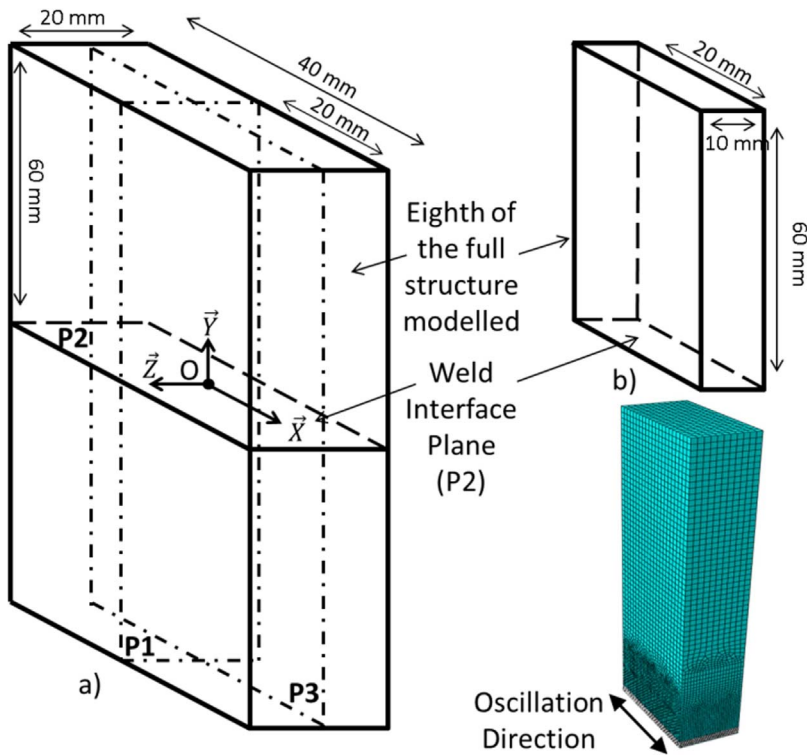


Fig. 4. a) Schematic diagram of the full LFW structure with its planes of symmetry, P1, P2 and P3 and b) geometry showing how only an eighth of the sample was modelled with the corresponding mesh.

where  $T_{phase}$  is the duration of the phase being considered,  $F_{int}$  the force at the weld interface and  $v$  the velocity of the oscillating workpiece. Using the machine data for the five different sets of welding parameters in Table 1, five models were built.

## 2.2. Modelling approach

To avoid modelling the oscillations an accurate heat flux must be applied to the weld region and elements iteratively removed from the interface to account for the burn-off. The following sections describe the four key areas.

## 2.3. Mesh and material properties

As shown in Fig. 1 the real workpieces are  $20 \times 40 \times 120$  mm. Deformation and heat flow are approximately symmetric around the planes (P1), (P2) and (P3), see Fig. 4(a), therefore only an eighth of the geometry was included. As a result, a workpiece measuring  $10 \times 20 \times 60$  mm was modelled using the FEA software ABAQUS, see Fig. 4(b). The mesh is composed of eight-node linear heat transfer bricks. Fine elements are needed at the weld interface and its vicinity to ensure that steep thermal gradients are captured by the numerical model. To determine the level of discretisation needed, a mesh sensitivity study was conducted on weld 4 (welding conditions presented in Table 1), see Table 2. The mesh element lengths displayed in Table 2 refer to a band of material located within 6.6 mm back from the weld

interface. Further away from this, the mesh is coarsened to 1 mm. The predictions of the peak temperature in Table 2 indicate that a minimum size of 0.3 mm is required within the 6.6 mm band to capture an accurate thermal profile. Ti-6Al-4V temperature dependent specific heat and conductivity from the DEFORM's software library are used in the model.

## 2.4. Application of the heat flux and modelling of the burn-off

Since the oscillations are not modelled, it is necessary to find an alternative way to account for the heat generation. To do so, the average heat flux for each phase was estimated by post-processing the machine data obtained when making a linear friction weld, as previously described. In accordance with the literature (Turner et al., 2011), 100% of the mechanical energy is assumed to be transformed into heat. A uniform surface heat flux ( $W m^{-2}$ ) was applied on the weld interface during phase 1 and 2. Indeed, during phase 1 only dry friction occurs while phase 2 is a much shorter phase in comparison with phases 1 and 3, where a transition between dry to sticking friction occurs. Therefore, application of the heat flux to the surface is a reasonable assumption for the first two phases. However, the heat is generated by the plastic deformation within the material during phase 3 over the TMAZ (thermo-mechanically affected zone), implying a volumetric generation of heat. A study of the influence of the phase 3 volumetric heat distribution is performed on welds 1 and 4 from Table 1, by considering three different heat distributions, shown in Fig. 5. As for phases 1 and 2, a surface heat flux was considered for phase 3, as well as two volumetric heat distributions, one is distributed over half the TMAZ and the second one was distributed over the whole TMAZ. TMAZ thicknesses were calculated using an equation from McAndrew et al. (2015a, 2015b). As will be proved in the results, a surface heat flux was shown to be adequate and was used for the subsequent modelling work. Since deformation of the workpieces is not included in the model, it does not capture the effects of strain-rate and plastic work. Nevertheless, these efforts are indirectly included with the heat flux calculated from the machine data.

Modelling the burn-off during the process is important during phase

Table 2  
Mesh sensitivity results.

Mesh element length (mm)	Total number of elements	Interface temperature prior cooling (°C)
0.7	31350	983
0.5	43313	986
0.3	98165	994
0.2	234417	994



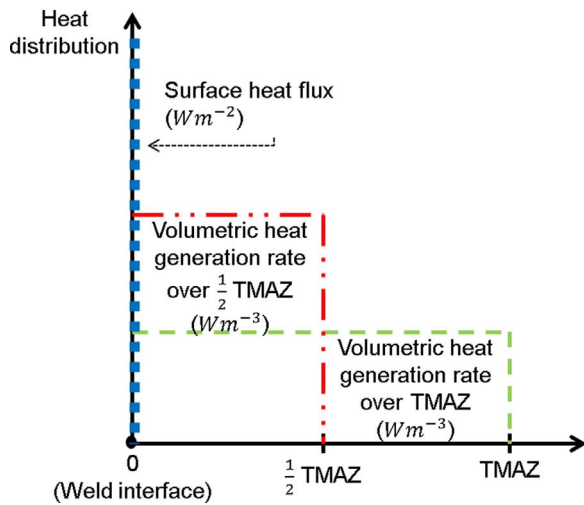


Fig. 5. Three types of heat distributions investigated for phase 3.

3 in particular, where it allows the temperature and the in-plane force distributions across the interface to reach a quasi-steady state. The burn-off is modelled in a step-wise approach where rows of elements are removed at a pace which matches the experimental burn-off rate. Fig. 6 illustrates this approach with the heat flux applied during step 1 then a row of elements is removed during step 2 and the heat flux is reapplied. For a typical burn-off value of 1.5 mm (3 mm total), 10 steps are required for removal, with each layer being 0.15 mm thick. Hence the thickness of the elements that are removed as part of the burn-off is smaller than the 0.3 mm thickness used for the surrounding elements. Note that the effect of the number of steps on the thermal profile was investigated, where the material was removed in 1, 5, 10 and 20 steps.

### 2.5. Additional data

The trend of the equilibrium heat flux and the weld interface temperature against the burn-off rate is analysed in the results section. In addition to the welds presented Table 1, machine data from experimental trials conducted by McAndrew et al. (2014), presented in Table 3, were post-processed and a simulation of each was created using the modelling approach presented in this chapter. The coupon dimensions used by McAndrew are the same as those used earlier, see Fig. 1. Values of equilibrium heat flux and burn-off rate of the welds presented Table 1 are given in Table 4.

## 3. Results and discussion

### 3.1. Effects of the heat flux distribution and steps for element removal

Temperature profiles predicted at the end of phase 3 using the three

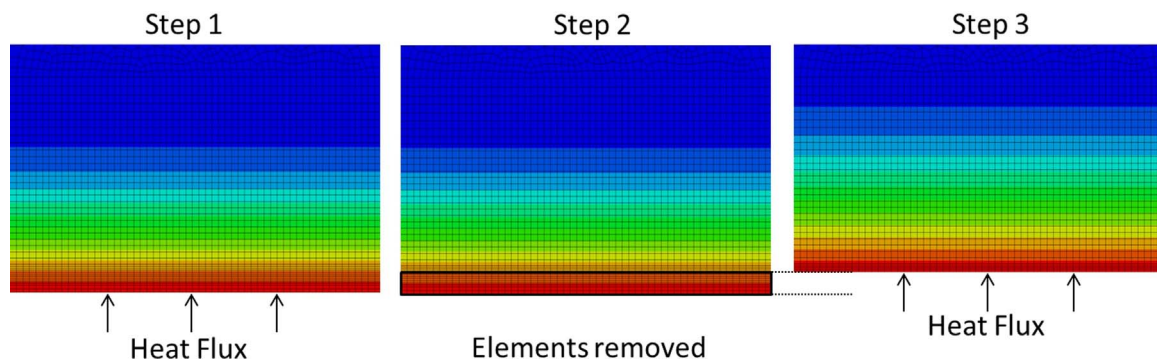


Fig. 6. Step-wise removal approach.

Table 3

Experimental conditions used by McAndrew et al. (2014).

Weld	Freq. (Hz)	Amp. (mm)	Applied pressure (MPa)	Burn-off (mm)	Heat flux (kW)	Burn-off rate (mm/s)
9	30	2	40	3	7.37	2.09
10	50	2.7	40	3	12.08	4.1
13	30	1	125	3	4.22	1.1
16	31.6	2.3	85.3	2.5	9.57	3.16
21	30	2	40	3	7.33	2
25	30	1	125	3	4.15	1.15

Table 4

Heat flux and burn-off rate for the experimental conditions in Table 1.

Weld	Heat flux (kW)	Burn-off rate (mm/s)
1	4.29	1.25
2	8.77	2.72
3	12.81	4.12
4	12.66	4.97
5	16.1	6.3
6	8.57	2.63
7	12.53	5.21
8	12.77	5.23

heat flux distributions for the low rubbing velocity condition, weld 1 and the high rubbing velocity condition, weld 4 are displayed Fig. 7. The thermocouple signal was lost before reaching phase 3 for weld 1; therefore measurements were only added for weld 4 in Fig. 7(b). The temperatures predicted are shown to be largely independent of the heat distribution with the greatest difference occurring at the weld interface. The volumetric heat distribution over the whole TMAZ resulted in a lower peak temperature and a shallower temperature gradient at the vicinity of the interface due to the wider distribution of heat. Moreover, the equation used to calculate the TMAZ thickness (McAndrew et al., 2015a, 2015b), which is based on results from FEA models, tends to over-predict their values compared to the experiments. Therefore having a larger predicted TMAZ, will enhance the small differences between thermal profiles predicted in Fig. 7. Based on this study, a surface heat flux will be used for all subsequent modelling work since the size of the TMAZ is not required, simplifying the analysis.

The influence of removing the total burn-off in 1, 5, 10 and 20 steps on the final thermal profile of phase 3, for welds 1 and 4 is displayed Fig. 8. As stated previously, thermocouple measurements are only presented for weld 4 in Fig. 8(b). The number of steps has a greater effect for the high rubbing velocity weld 4 due to the steep thermal gradients created for this welding condition. It can be seen that deleting the 1.5 mm of burn-off in 1 step will under predict the interface temperature for both welds. Beyond 5 steps, all the thermal profiles converge toward the same distribution, so using 10 steps will be sufficiently

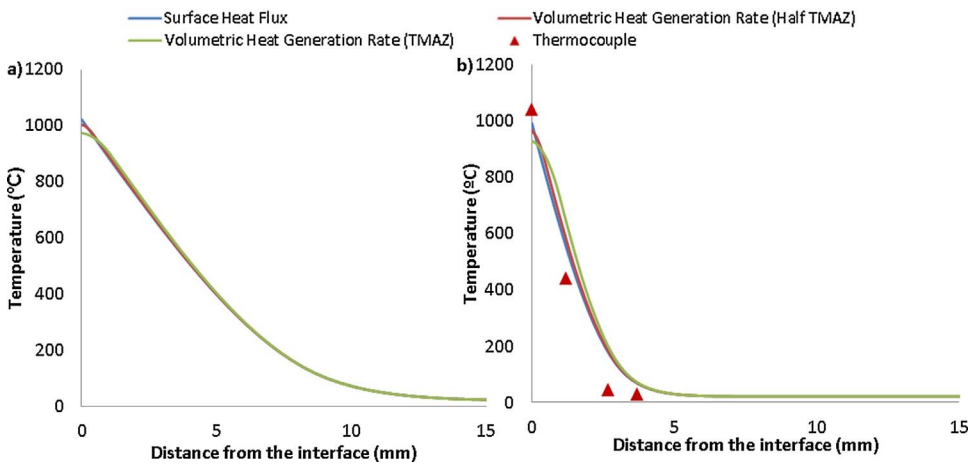


Fig. 7. Comparison of the thermal profiles obtained at the end of phase 3 for different heat flux distributions: a) weld 1 and b) weld 4.

large to have no impact on the temperature distribution and provides a good match against the thermocouple recordings.

### 3.2. Effects of the LFW processing conditions

#### 3.2.1. Influence of the rubbing velocity

Thermal histories experimentally recorded and predicted by the numerical model for three welding conditions are displayed Fig. 9. Despite the groove present to facilitate the passage of the wires, some of the thermocouples broke during welding. Consequently, some temperature histories are missing. An applied pressure of 90 MPa is maintained for all the welds, while rubbing velocities of 120 mm/s, 240 mm/s and 540 mm/s were used for weld 1, weld 2 and weld 4. Fig. 9 displays a reasonable agreement between experiments and simulations, demonstrating the ability of the modelling approach to capture actual thermal histories while bypassing the oscillating motion of the workpieces. Nevertheless, discrepancies may have arisen from the positioning of the thermocouples since the thermal gradients generated during the LFW process are very high. In addition, uncertainties also arise from the measurement quality of the material properties used in the models. The largest discrepancies arise where the thermocouples are positioned the furthest. This may suggest that thermocouple wires got pulled away from their initial positions during welding and because of the high thermal gradient created, even a small offset in the original position would result in a significant discrepancy. Finally, there is an oscillation in the temperature predicted 0.3 mm from the weld interface in the results presented Fig. 9. This is due to the approach used to account for the axial shortening with the step-wise removal of elements and is therefore a modelling artefact. However, it shows that this step-

wise removal approach of material manages to capture the quasi-static state of the weld interface temperature.

The maximum interface temperature of welds 1, 2 and 4 are 1022 °C, 1111 °C and 994 °C. Both, experiment and simulation demonstrate that increasing the rubbing velocity does not necessarily result in an increase of the interface temperature. This fact is in contrast with the results predicted by the numerical model of McAndrew et al. (2015a, 2015b), where an increase in the rubbing velocity resulted in an increase of the weld interface temperature, see Fig. 10. Schroeder et al. (2015) confirmed the effect of the rubbing velocity highlighted by McAndrew with his numerical model and thermocouple recordings. However, Li et al. (2010) developed a 2D model where increasing the rubbing velocity did not affect the weld interface temperature. These peak temperature predictions are compared in Fig. 10, which shows an increase of the weld interface temperature when increasing the rubbing velocity, for the rubbing velocities under 480 mm/s. However, Turner et al. (2011) model predicted a similar weld interface temperature for the rubbing velocities above 480 mm/s. Differences between the results may have arisen from the different modelling approaches used by the authors as well as the different workpiece geometries and material properties considered.

These divergent results highlight that the trend of the interface temperature cannot be predicted by looking only at the rubbing velocity. The behaviour of the process during the equilibrium phase is crucial to understanding these temperature differences. The interface temperature is determined by the balance between the heat input during this phase and the speed at which the hot material is removed from the interface, i.e. the burn-off rate.

In the case of weld 1, both the average heat flux of phase 3 and the

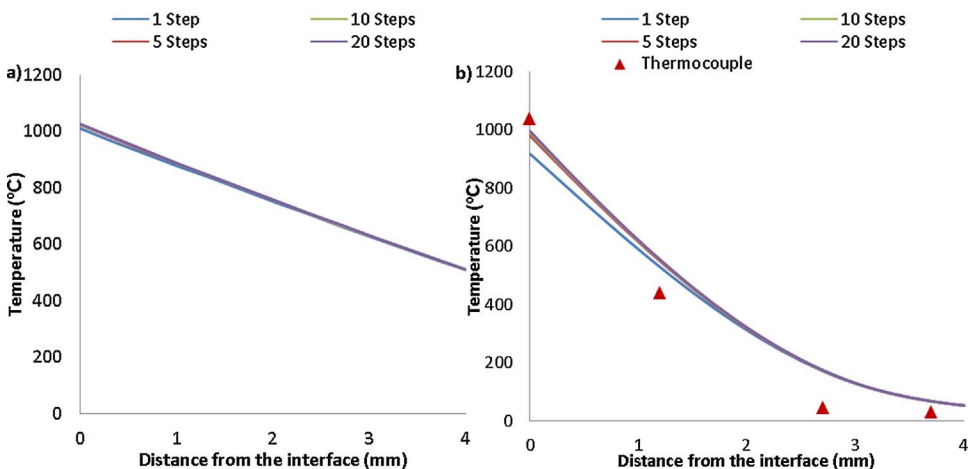


Fig. 8. Influence of the number of steps to model the burn-off for: a) weld 1 and b) weld 4.

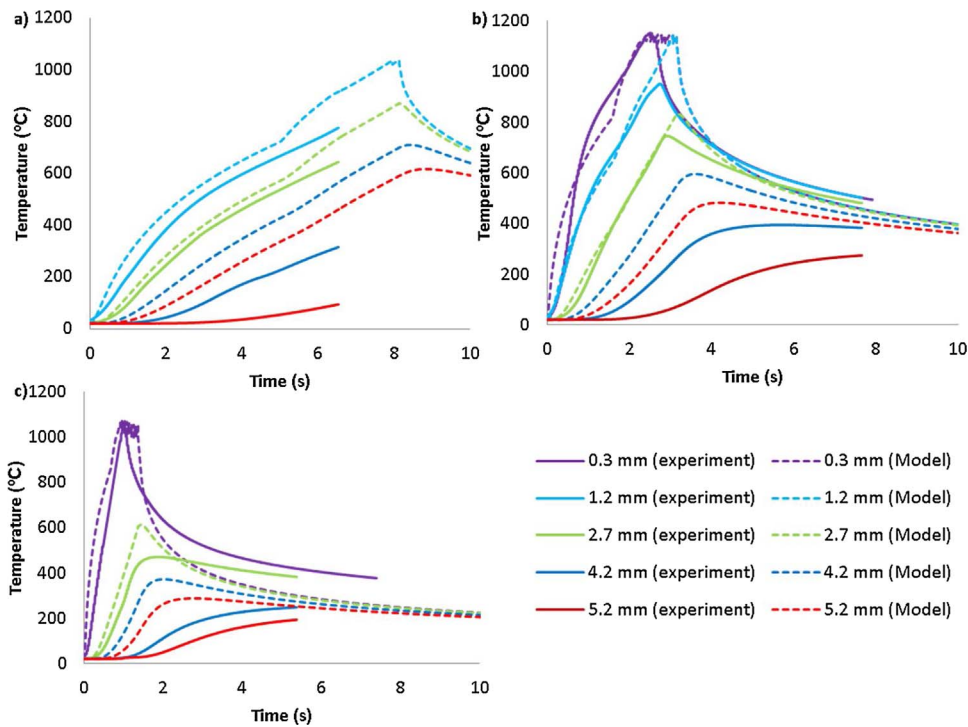


Fig. 9. Comparison of thermal histories obtained from experiments and FEA simulations for three sets of welding conditions: a) weld 1 ( $\nu_r = 120$  mm/s), b) weld 2 ( $\nu_r = 240$  mm/s) and c) weld 4 ( $\nu_r = 540$  mm/s).

burn-off rate are low, as seen Table 4. This condition results in a slow heat up of the weld interface and more heat loss due to conduction into the surrounding cold material, creating a low thermal gradient, see Fig. 11. Fig. 11, shows that increasing the rubbing velocity at a constant applied pressure results in an increase of the thermal gradient. A similar trend can be observed in the works of McAndrew et al. (2015a, 2015b) and Turner et al. (2011). In contrast to weld 1, weld 4 heat flux and burn-off rate are considerably higher. However, despite the high weld 4 heat flux, the temperature cannot build-up at the weld interface since the hot material is removed at a high rate, creating a steep thermal gradient, see Fig. 11. Weld 2 offers a compromise between weld 1 and 4 in terms of heat flux and burn-off rate, which produced a higher temperature at the weld interface.

### 3.2.2. A method to estimate the weld interface temperature

To provide further evidence for the variation in peak temperature with rubbing velocity, models were built for the welding trials conducted by McAndrew et al. (2014) displayed in Table 3. The burn-off rate is considered rather than the rubbing velocity so data from welds

with different applied pressure can be integrated into the study.

The evolution of the equilibrium heat flux and the weld interface temperature against the burn-off rate are presented Fig. 12. For both plots, an equation of the trend with its R-squared ( $R^2$ ) value is provided. It can be seen that the equilibrium heat flux increases when increasing the burn-off rate. An increase in the burn-off rate can be achieved in three ways. It can be due to either an increase in rubbing velocity or applied pressure or oscillating in the short rather than long direction. In the first case, the heat flux is linearly dependant on the velocity of the moving workpiece so an increase in the rubbing velocity results in an increase in the heat flux magnitude. However, when oscillating in the shortest direction or increasing the applied pressure, the rubbing velocity is unchanged. In these cases the heat flux increases because more cold material is introduced to the weld interface. As detailed by McAndrew et al. (2015a, 2015b), the greater heat flux is caused by a larger friction force due to an increase in the flow stress as a consequence of the colder deforming material.

As stated previously, the peak temperature is determined by a balance between equilibrium heat flux and burn-off rate. The highest

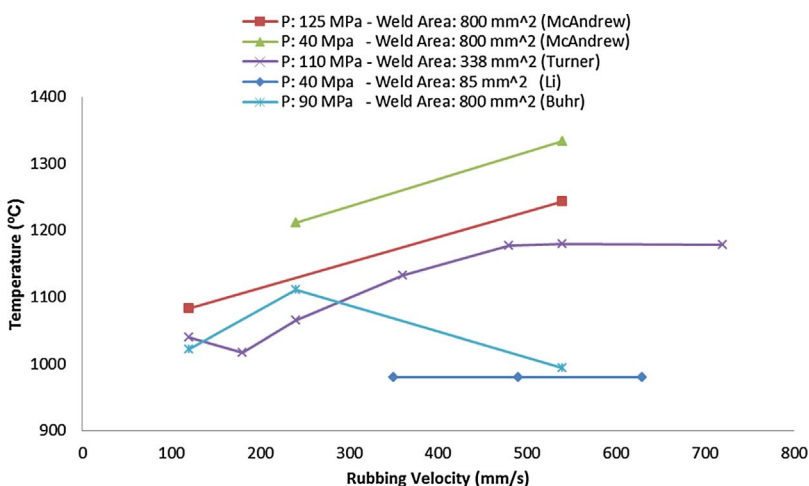


Fig. 10. Evolution of the weld interface temperature during the equilibrium phase against the rubbing velocity predicted by: McAndrew et al. (2015a, 2015b), Turner et al. (2011) and Li et al. (2010).

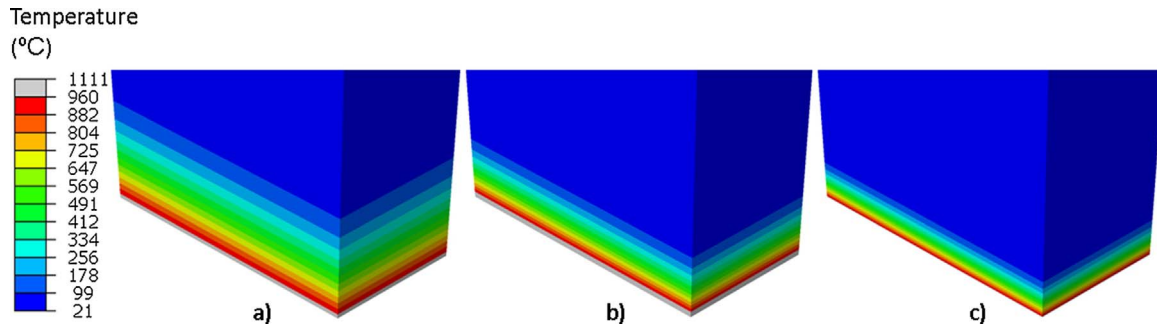


Fig. 11. Thermal profiles, during phase 3 for: a) weld 1 ( $v_r = 120$  mm/s), b) weld 2 ( $v_r = 240$  mm/s) and c) weld 4 ( $v_r = 540$  mm/s).

interface temperature is reached for a burn-off rate between 2 and 3 mm/s while increasing or decreasing the burn-off rate outside this, results in a drop of temperature. This trend in the temperature confirms the results obtained in the previous section on the influence of the rubbing velocity. Based on Fig. 12, it is possible to estimate the magnitude of the weld interface temperature obtained at the end of phase 3, without using thermocouples or a numerical model, from the experimental burn-off rate or the equilibrium heat flux. It is worth mentioning that Fig. 12 is only valid for the workpiece geometry used in this study.

To understand the contributions of heat lost by conduction and lost in the flash, a heat balance over a control volume around the weld interface can be developed:

$$Q_{Total} = Q_{in} - Q_{conduction} - Q_{flash}$$

where  $Q_{Total}$  is the total energy contained in the control volume,  $Q_{in}$  is the energy brought in the control volume by sliding or plastic work,  $Q_{conduction}$  is the energy lost by conduction and  $Q_{flash}$  is the energy lost in the flash.

When the process is in steady-state, this equation simplifies to the following after differentiating with respect to time:

$$\dot{Q}_{conduction} = \dot{Q}_{in} - \dot{Q}_{flash}$$

Indeed, since the temperature field reaches a quasi-steady state,  $\dot{Q}_{Total}$  is nil. Furthermore,  $\dot{Q}_{in}$  represents the average equilibrium heat flux, previously calculated from the post-processing of the machine data, while is given by:

$\dot{Q}_{flash} = \rho \cdot A \cdot c_p \cdot BoR \cdot (T_{flash} - T_{init})$  where  $\rho$  is the density,  $A$  the area of the weld cross-section,  $c_p$  the specific heat capacity (an average value of 690 J/(Kg.K) is used),  $BoR$  the burn-off rate,  $T_{flash}$  the temperature of the flash (taken at 1000 °C) and  $T_{init}$  the temperature of the workpieces prior welding.

Fig. 13(a) displays the evolution of the magnitudes of the heat fluxes acting in and out of the control volume against the burn-off rate. The heat flux responsible for heat losses in the flash increases linearly with the burn-off rate like  $\dot{Q}_{in}$ , which provides energy to the weld. However, the heat loss due to conduction is largely independent of the burn-off rate used. Fig. 13(b) displays the magnitude of the heat fluxes lost in the flash and by conduction, expressed as a percentage of  $\dot{Q}_{in}$ . The objective

of Fig. 13(b) is to quantify the contribution of the two mechanisms responsible for heat losses in the control volume. It can be observed that for burn-off rates less than about 3 mm/s, the heat flux lost by conduction represents about 30% of the total required to make the weld. Above a 3 mm/s burn-off rate, the contribution of conduction decreases to a value of about 6%. Therefore conduction has much greater impact on the temperature field at low burn-off rates. If conduction is ignored, the power to make a weld can be estimated from the energy required to produce the flash.

As previously mentioned, an increase in the applied pressure is known to increase the burn-off rate (see Table 4 burn-off rate values, weld 3 versus weld 4 where the applied pressure increases from 40 MPa to 90 MPa). However it is possible to reduce the peak temperature by reducing the applied pressure and the burn-off rate according to the relationship in Fig. 12. This would contradict McAndrew et al. (2015) and Turner et al. (2012) findings. McAndrew et al. (2015a, 2015b) established that a decrease in the applied pressure has a small impact on the experimental phase 3 heat flux. Furthermore, using McAndrew et al. (2015a, 2015b) equation which predicts experimental burn-off rates, the evolution of the burn-off rate is plotted against the applied pressure for different rubbing velocity conditions in Fig. 14 (the amplitude is kept constant at 3 mm while the frequency varies from 10 Hz to 50 Hz). This demonstrates that the burn-off rate is largely independent of the applied pressure for low rubbing velocities. Hence, low burn-off rates can only be achieved by reducing the rubbing velocity and not the applied pressure. Consequently, if the initial burn-off rate is 2 mm/s and the applied pressure is decreased, it will not affect the burn-off rate or the phase 3 power; therefore the weld interface temperature will be unchanged.

### 3.2.3. Influence of the applied pressure

Comparisons of thermal histories between experiments and simulations, for weld 3 and weld 4, are displayed in Fig. 15. Both welds were made with a rubbing velocity of 540 mm/s while using an applied pressure of 40 MPa for weld 3 and 90 MPa for weld 4. A reasonable

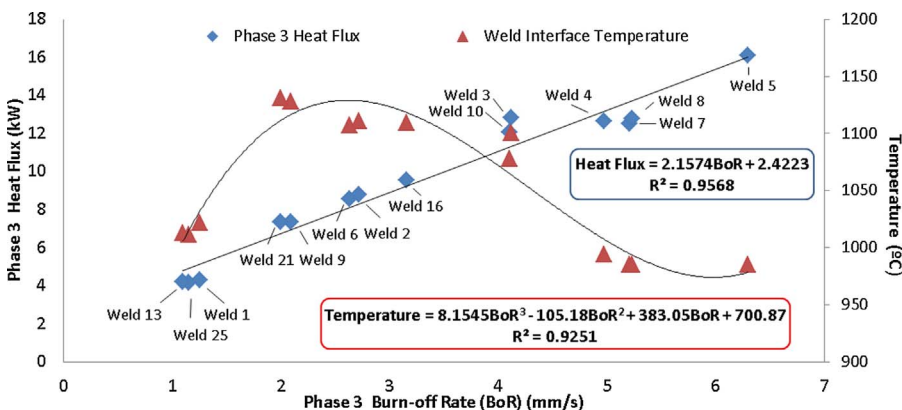


Fig. 12. Evolution of the phase 3 heat flux and the equilibrium weld interface temperature against the burn-off rate.



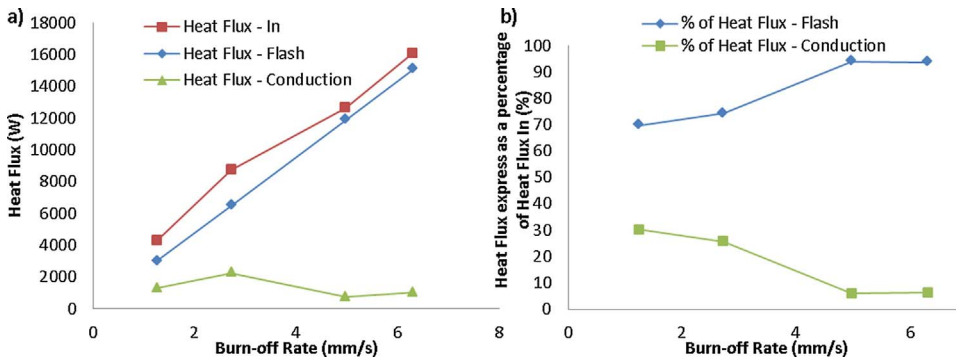


Fig. 13. a) Evolution of the heat flux magnitudes, acting in and out of a control volume, against the burn-off rate and b) contribution of the heat fluxes from the flash and conduction expressed as a percentage of the heat flux in.

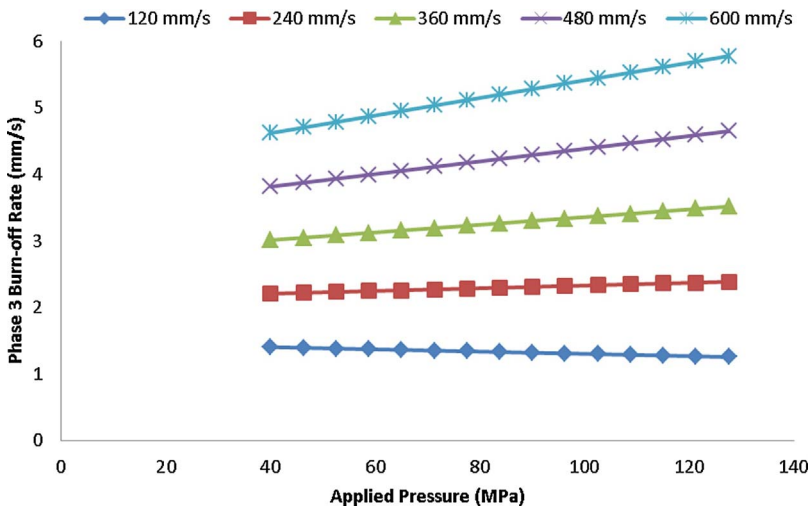


Fig. 14. Evolution of the burn-off rate against the applied pressure for different rubbing velocities (obtained from McAndrew et al. (2015a, 2015b) equation).

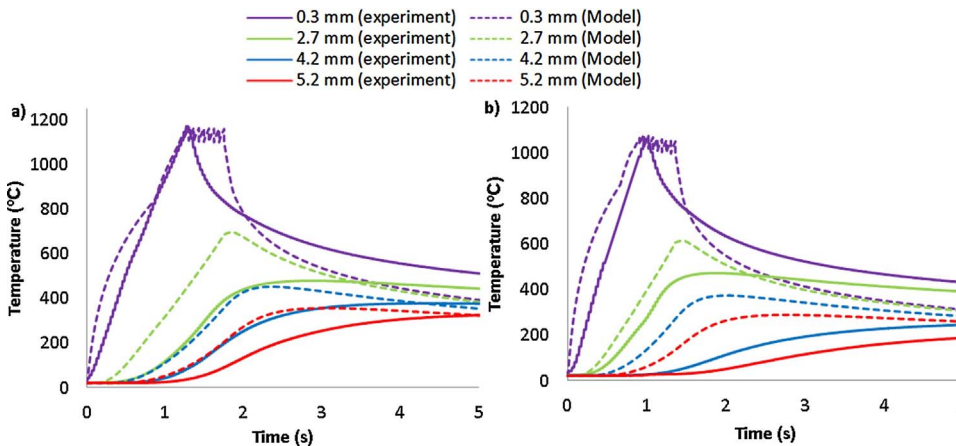


Fig. 15. Thermal histories obtained from experiments and FEA for two sets of experimental conditions where only the applied pressure changes: a) weld 3 ( $P = 40$  MPa) and b) weld 4 ( $P = 90$  MPa).

match between experiments and simulations is observed. A higher maximum temperature is reached for the lower applied pressure weld 3 compared to weld 4 reaching 1170 °C and 994 °C respectively. The same trend was observed by McAndrew et al. (2015a, 2015b) and Turner et al. (2012). Looking at Table 4, the applied pressure of 40 MPa compared with 90 MPa had virtually no impact on the heat flux, with a variation of about 1%, however it decreased the burn-off rate by about 17%. Therefore, for an equivalent heat flux, the hot material was left a longer time at the weld interface, allowing the temperature to build-up. It is worth noticing that even if the burn-off rate of weld 3 is lower than weld 4, it is still substantially higher than the burn-off rate of weld 1 (over three times higher) and the temperature at the interface does not have time to conduct back to the same extent.

### 3.2.4. Influence of the oscillation direction

Temperature histories of weld 4 and 5 are displayed Fig. 16, where the oscillating workpiece was oscillated respectively in the 40 mm and 20 mm directions of the workpiece. As shown in Fig. 16, a slightly cooler weld is produced when oscillating in the 20 mm direction. As shown in Table 4, the sample that was oscillated in the 20 mm direction (i.e. weld 5) had a 27% higher burn-off rate compared to weld 4 despite having the same rubbing velocity which is in agreement with McAndrew et al. (2016). Oscillating in the 20 mm direction facilitates the expulsion of the material since the material has less distance to travel to form the flash. In addition, the equilibrium heat flux of weld 5 is 27% higher compared to weld 4, which explains why weld 4 and weld 5 have similar weld interface temperatures.

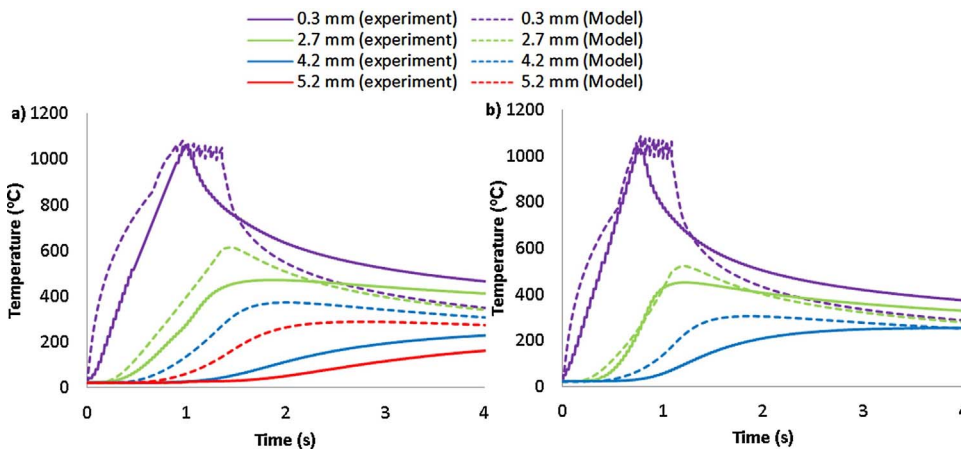


Fig. 16. Thermal histories obtained from experiments and FEA for two sets of experimental conditions where only the oscillation direction changes: a) weld 4 (40 mm direction) and b) weld 5 (20 mm direction).

#### 4. Conclusions

The key findings from this work are:

1. A novel LFW process model that bypasses the need to dynamically model the oscillations was developed. The advantage of this modelling approach is that thermal profiles can be obtained quickly for subsequent residual stress modelling.
2. In general, the thermal profiles generated by the model are in good agreement with the thermocouple measurements, therefore suggesting the model captures the process trends well.
3. According to the model, the weld interface temperature does not necessarily increase with the rubbing velocity. Moreover, applying a high pressure or oscillating the workpiece along the shorter of the two interface dimensions produces a cooler interface temperature. Overall, the interface temperature can be explained by a balance between heat generation and the heat lost as a consequence of the flash generation.
4. A maximum weld interface temperature is reached for burn-off rate values between 2 and 3 mm/s, for the workpiece geometry used in this study.

#### Acknowledgements

The authors would like to thank the Honeywell Company and Cranfield University for funding the research presented in that paper. Also, the help provided by Bertrand Flipo of The Welding Institute (TWI) in conducting the experiments was greatly appreciated.

#### References

- Addison, A., 2008. Linear friction welding of engineering metals. TWI Ind. Memb. Rep. 894.
- Blau, P.J., 2001. The significance and use of the friction coefficient. *Tribol. Int.* 34, 585–591.
- Grant, B., Preuss, M., Withers, P.J., Baxter, G., Rowson, M., 2009. Finite element process modelling of inertia friction welding advanced nickel-based superalloy. *Mater. Sci. Eng. A* 513–514, 366–375.
- Kumar, B.V.R.R., 2013. A review on blisk technology. *Int. J. Innov. Res. Sci. Eng. Technol.* 2, 1353–1358.
- Li, W.-Y., Ma, T., Li, J., 2010. Numerical simulation of linear friction welding of titanium alloy: effects of processing parameters. *Mater. Des.* 31, 1497–1507.
- Li, W., Wu, H., Ma, T., Yang, C., Chen, Z., 2012. Influence of parent metal microstructure and post-weld heat treatment on microstructure and mechanical properties of linear friction welded Ti-6Al-4V joint. *Adv. Eng. Mater.* 14, 312–318.
- Li, W., Vairis, A., Preuss, M., Ma, T., 2016. Linear and rotary friction welding review. *Int. Mater. Rev.* 61, 71–100.
- McAndrew, A.R., Colegrove, P.A., Addison, A.C., Flipo, B.C.D., Russell, M.J., 2014. Energy and force analysis of Ti-6Al-4V linear friction welds for computational modeling input and validation data. *Metall. Mater. Trans. A* 45, 6118–6128.
- McAndrew, A.R., Colegrove, P.A., Addison, A.C., Flipo, B.C.D., Russell, M.J., 2015a. Modelling the influence of the process inputs on the removal of surface contaminants from Ti-6Al-4V linear friction welds. *Mater. Des.* 66, 183–195.
- McAndrew, A.R., Colegrove, P.A., Addison, A.C., Flipo, B.C.D., Russell, M.J., Lee, L.A., 2015b. Modelling of the workpiece geometry effects on Ti-6Al-4V linear friction welds. *Mater. Des.* 87, 1087–1099.
- McAndrew, A.R., Colegrove, P.A., Flipo, B.C.D., Bühr, C., 2016. 3D modelling of Ti-6Al-4V linear friction welds. *Sci. Technol. Weld. Join.* 1718, 1–9.
- Ofem, U.U., Colegrove, P.A., Addison, A., Russell, M.J., 2010. Energy and force analysis of linear friction welds in medium carbon steel. *Sci. Technol. Weld. Join.* 15, 479–485.
- Romero, J., Attallah, M.M., Preuss, M., Karadge, M., Bray, S.E., 2009. Effect of the forging pressure on the microstructure and residual stress development in Ti-6Al-4V linear friction welds. *Acta Mater.* 57, 5582–5592.
- Schroeder, F., Ward, R.M., Turner, R.P., Attallah, M.M., Gebelin, J., Reed, R.C., 2012. Linear friction welding of titanium alloys for aeroengine applications: modelling and validation. 9th Int Conf. Trends Weld. Res. 886–892.
- Schroeder, F., Ward, R.M., Turner, R.P., Walpole, A.R., Attallah, M.M., Gebelin, J.-C., Reed, R.C., 2015. Validation of a model of linear friction welding of Ti6Al4V by considering welds of different sizes. *Metall. Mater. Trans. B* 46, 2326–2331.
- Turner, R., Gebelin, J.-C., Ward, R.M., Reed, R.C., 2011. Linear friction welding of Ti-6Al-4V: modelling and validation. *Acta Mater.* 59, 3792–3803.
- Turner, R., Ward, R.M., March, R., Reed, R.C., 2012. The magnitude and origin of residual stress in Ti-6Al-4V linear friction welds: an investigation by validated numerical modeling. *Metall. Mater. Trans. B* 43, 186–197.
- Vairis, A., Frost, M., 1998. High frequency linear friction welding of a titanium alloy. *Wear* 217, 117–131.
- Vairis, A., Frost, M., 2000. Modelling the linear friction welding of titanium blocks. *Mater. Sci. Eng. A* 292, 8–17.
- Wang, X.Y., Li, W.Y., Ma, T.J., Vairis, A., 2017. Characterisation studies of linear friction welded titanium joints. *Mater. Des.* 116, 115–126.
- Wanjara, P., Jahazi, M., 2005. Linear friction welding of Ti-6Al-4V: processing, microstructure, and mechanical-property inter-relationships. *Metall. Mater. Trans. A* 36, 2149–2164.

# A computationally efficient thermal modelling approach of the linear friction welding process

Buhr, Clement

2017-09-14

Attribution 4.0 International

---

Buhr C, Colegrove PA, McAndrew AR. (2018) A computationally efficient thermal modelling approach of the linear friction welding process. *Journal of Materials Processing Technology*, Volume 252, February 2018, pp. 849-858

<http://dx.doi.org/10.1016/j.jmatprotec.2017.09.013>

*Downloaded from CERES Research Repository, Cranfield University*